Grid-Free Simulation of the Spatially Growing Turbulent Mixing Layer

Peter S. Bernard*
University of Maryland, College Park, Maryland 20742

The spatially developing, unforced, turbulent mixing layer is simulated via a grid-free vortex method. Vortex filaments composed of straight tubes are used as the computational element with new vortex tubes produced as the filaments stretch. A loop removal algorithm serves as a de facto subgrid model limiting growth in the number of elements to practical levels. The computations are high resolution and well resolve the mixing layer from its unforced inception as a laminar flow through transition to a self-similar turbulent state. Mean velocity statistics including growth rate and Reynolds stresses agree well with experimental values. The vortical composition of the transition region is found to develop in one or another of the modes that have been documented in previous experiments and computations: roller/rib vortices, the chain-link fence structure in a diamond shaped pattern, and somewhat oblique roller/rib configuration with partial pairing. Evidently, small perturbative effects that are intrinsic to the numerical scheme influence which transitional mode appears locally in the simulations. The computations offer a clear view of the downstream dissolution of the identifiable structure into turbulence in the late transition and the salient aspects of the process are noted.

Nomenclature

h	=	maximum vortex tube length
L	=	downstream boundary
l	=	similarity length scale
N	=	number of vortex tubes
R_x	=	boundary layer Reynolds number
$\mathbf{s}_i$	=	axial vector along the ith vortex tube
U_{in}	=	inlet velocity
$\mathbf{U}_p(\mathbf{x}, t)$	=	potential velocity
U_t, U_b	=	velocities at top and bottom of shear layer
x, y, z	=	streamwise, vertical, and spanwise coordinates
$\mathbf{x}_i$	=	center of ith vortex tube
$\mathbf{x}_i^1, \mathbf{x}_i^2$	=	beginning and end of ith vortex tube
Γ_i	=	circulation of ith vortex tube
ε	=	vertical offset of downstream vortex sheet
η	=	similarity variable
θ	=	momentum thickness
σ	=	smoothing parameter
ϕ	=	smoothing function

I. Introduction

THE high Reynolds number spatially developing mixing layer formed at the juncture of two parallel streams of unequal velocity is of intrinsic interest both as a fundamental example of shear induced turbulence as well as an important component of many complex, engineering flows. Building on earlier studies, physical experiments such as those of Lasheras et al. [1], Lasheras and Choi [2], Bell and Mehta [3], Leboeuf and Mehta [4], and Slessor et al. [5], as well as numerical work by Rogers and Moser [6,7], Comte et al. [8,9], Collis et al. [10], and Ansari [11], among others, have yielded considerable understanding of the mixing layer physics including its vortical makeup during transition and the statistical properties of the downstream fully turbulent, self-similar flow.

A backdrop to much of what is known about the mixing layer is the understanding that it is sensitive to inlet conditions such as turbulence levels and imposed forcings that affect both the way in which the transitional vortex system develops as well as flow statistics measured in the self-similar region. Several modes of vortex behavior have been observed in the transition region: a system of spanwise roller and streamwise rib vortices associated with the Kelvin–Helmholtz instability [1,2,4,6], a lattice structure reminiscent of a chain-link fence that is associated with spanwise asymmetrical perturbations [10,12], and what may be described as a three-dimensional variant of the roller/rib forms with partial pairing and branching of vortices that may follow from turbulent inlet conditions [8,9,13]. Regardless of the transition, the self-similar turbulent shear layer is characterized by linear growth of the momentum thickness and collapsing velocity statistics though growth rates and Reynolds stress amplitudes are well known to vary from one experiment to another [14]. Evidently, the downstream persistence of at least some aspects of the inlet conditions, as reflected in particular characteristics of the vortices in the transition region, has a bearing on the properties of the self-similar flow [5,15].

Further understanding of the mixing layer is perhaps most required in regards to the circumstances surrounding its entire spatial development from inlet through transition to self-similar turbulent flow. For example, it is not entirely clear when or in what way to expect the appearance of different transition modes within a given mixing layer, nor their relationship to the downstream turbulent flow. Insights along these lines are likely to be most readily obtained from the special capabilities of numerical schemes in supplying detailed information about flow structure and statistics. To shed light on these issues requires a numerical simulation capable of providing a more complete view of the spatial mixing layer than has yet been achieved. In this work it will be seen that a useful tool for simulating the spatially growing mixing layer lies in a grid-free vortex filament method incorporating an implicit "subgrid" model in the form of a loop removal algorithm [16].

Many of the benefits of simulation that have been realized to date, such as detailed reconstructions of the vortex dynamics in the transition region and insights into the connection between inlet conditions and the downstream self-similar flow, have been obtained from the closely related transient mixing layer. To some extent this reflects the numerical advantages that accrue from the opportunity to invoke streamwise periodicity. Studies of the transient flow overlook features unique to the spatially developing case such as the simultaneous presence of the various flow stages that naturally feed back to the inlet and the bending of the mixing layer toward the slow side [17–19]. Direct treatment of the spatially growing case also

*Professor, Department of Mechanical Engineering. Member AIAA.

eliminates the potential for ambiguity arising from the selection of an appropriate convection velocity for use with Taylor's hypothesis [20,21].

Numerical simulations of the spatially developing mixing layer have also been made, though such computations have generally been of limited scope and purpose. For example, Druzhinin and Elghobashi [22] calculated a mixing layer at relatively low Reynolds number with the primary interest of looking at the dynamics of embedded bubbles. Special forcing at the inlet was used to create streamwise vortices and the computed flow did not extend far enough in the streamwise direction to have a clear-cut self-similar region. At a somewhat higher Reynolds number Tenaud et al. [23] performed a large eddy simulation of a mixing layer with inlet velocity consisting of random noise superimposed on the mean flow exiting from a splitter plate. After adjustment of the subgrid model and amplitude of the inlet perturbations, the predicted growth rate was brought in line with physical experiments. A self-similar region was observed with properties that were in the range of experimental observations and brief consideration was given to the vortical structure that might be present.

The present work considers the numerical simulation of the spatially developing, unforced, turbulent mixing layer via a grid-free vortex method [16,24–26]. The Reynolds number is high and the field of vortices used in representing the flow is found to transition without forcing in response to whatever small perturbations may be present in the course of computing velocities used in determining the motion of the vortex system. Besides demonstrating the effectiveness of this approach in simulating an important shear flow by directly comparing computed results vs experiment, the intent is to add to the current understanding of the properties of the spatially developing mixing layer including the appearance of vortical modes in transition and the onset of turbulence. In particular, in the absence of purposeful forcing that would otherwise direct the solution toward one transition mode or another, it will be seen that all three transition modes seen in experiments can and do occur in the present calculations, thus affording an opportunity to gain some new insights into the complete range of behavior possible in the spatially developing mixing layer.

Vortex methods are attractive for studying the mixing layer and turbulent flows in general because they can accommodate high Reynolds number flow without concern for unwanted diffusion that may smooth regions of high shear. This advantage prompted early studies such as that of Ashurst and Meiburg [27] who modeled the transient mixing layer via a vortex filament method. Some insights into the formation of rib vortices and their connection to roller vortices were achieved despite coarse resolution in which single layers of filaments were used to represent the flow from the top and bottom of a splitter plate. Inoue [28] performed similar computations of the spatially growing mixing layer with a single layer of vortices. Somewhat better resolution was achieved by Knio and Ghoniem [29] in an application of the transport element method for a transient mixing layer. They examined the physics of the transition with five layers of vortices and introduced some degree of self-adaptivity by allowing for the creation of new vortices where called for in the calculation.

The development of schemes such as the fast multipole method [30] (FMM) and its practical implementation for vortex methods [31] has created the opportunity to perform substantially larger vortex method simulations than previously possible. In essence, the FMM reduces the nominal $\mathcal{O}(N^2)$ cost of evaluating velocities due to the mutual interactions of N vortices through the Biot–Savart law to a more manageable $\mathcal{O}(N)$ operation. High resolution studies of such flows as the two-dimensional cylinder wake [32] and three-dimensional sphere wake [33], among others, have illustrated the benefits of the vortex method for simulating high Reynolds number laminar flows. Depending on the particular formulation of the vortex scheme, the further extension of such methods to turbulent flows requires careful evaluation of vortex stretching effects to prevent instability or difficulties such as runaway growth in the number of new vortex elements. In the first approach toward simulating three-dimensional turbulence with a vortex method, Cottet et al. [34]

adopted a hybrid method in which vortex stretching was evaluated with the help of a mesh. Flow in a periodic box was simulated and shown to compare favorably with similar calculations using a spectral scheme.

The present study considers the simulation of the turbulent mixing layer via vortex filaments composed of straight tubes. The removal of vortex loops as they form provides an effective means of accommodating the physics of vortex stretching [16] within a grid-free context. A parallel implementation of the FMM is employed that enables practical computation with as many as 7 million vortex elements representing a gain of 2 orders of magnitude over previous vortex method applications to the mixing layer flow. It will be seen that this resolution is sufficient to encompass a significant mixing layer from the inlet through to a substantial self-similar region.

Sections II and III discuss in turn the numerical method and how it may be applied to the mixing layer. Section IV gives a consideration of statistical results, their comparison to experiments and how and to what extent they are sensitive to values of numerical parameters such as vortex length and domain length. Section V contains a discussion of the structural features of the simulated mixing layer followed by the conclusions.

II.   Computational Method

A.   Vortex Tubes

In this study, the evolving three-dimensional vorticity field is represented through the collective behavior of convecting and interacting vortical elements in the form of short, straight, vortex tubes joined end to end forming filaments. The ith vortex tube of N total is described via its circulation Γ_i and endpoints, say, $\mathbf{x}_i^1$ and $\mathbf{x}_i^2$. With the imposition of periodicity in the spanwise direction, it will be seen later that the filaments in effect extend to infinity so that violation of the divergence-free condition of the vorticity field is not a factor in these computations.

The dynamics of the vorticity field is modeled by convecting the endpoints of each tube via a simple Euler scheme and invoking Kelvin's theorem to justify preserving the circulation as a reasonable approximation in high Reynolds number flow. The elongation, rotation, and translation of the tubes via their endpoints provide an approximation to the stretching, reorientation, and convection effects in the equations of motion. The dominance of the vortex stretching process in turbulent flow causes vortex tubes to preferentially elongate in time. Consequently, to maintain the accuracy of the discretization the vortices are divided in half when they exceed a length, say h, that is assigned for each simulation. The importance of h in controlling the smoothness of the filaments as they fold and bend in the turbulent field will be shown in Sec. IV. In effect, h has a role in the grid-free calculation somewhat analogous to the mesh size appearing in grid-based methods.

Vortex stretching under turbulent flow conditions produces new vortex tubes at an extraordinarily fast rate so that unless special measures are taken to control the number of tubes the calculations will grow beyond practicality in a very short time. Chorin [35,36] observed that vortex stretching in the presence of bounded energy means that the filaments must preferentially fold, possibly forming loops because it is only in this way that a net far-field velocity can be prevented. The vortex loops can be associated with a local energy that would, if the numerical scheme permitted it, cascade to scales in the dissipation range to be then eliminated through the action of viscosity. Following a suggestion of Chorin [35,36], excision of vortex loops from the calculation as they form may function as a reasonable model of energy dissipation at the inertial range, thus saving a potentially costly calculation of the dynamics of the small scale motions. In effect, loop removal is tantamount to a de facto subgrid scale model, and so that by its inclusion the numerical scheme can be considered to have the characteristics of a large eddy simulation.

For loop removal to be a useful tool in turbulent flow simulation, it is necessary that it be sufficiently effective to prevent unbounded growth in the number of vortex elements. Moreover, it must do so in such a way that the physics of the resolved scales is left undisturbed.

These issues have been examined in a previous study of a turbulent puff of fluid created by pulsing a planar slot jet [16]. The results clearly establish the effectiveness of loop removal in limiting growth in the number of tubes without adverse effect on the turbulence simulation. In fact, whether or not loop removal was activated, the turbulence field was found to maintain a Kolmogorov $-5/3$ inertial range spectrum as well as structure functions, correlation functions, and isotropic flow properties consistent with experiments and theory. The loop removal algorithm is adopted in the present study, and, as will be seen below, it is found to also perform effectively in limiting the growth in the number of tubes while not appearing to have a detrimental effect on the resolved scales.

B. Velocity Computation

A central aspect of the numerical algorithm is the calculation of the velocity field associated with a given distribution of vortex tube elements. In principle, this entails a summation over the individual contributions of the N vortices according to the Biot–Savart law in combination with a potential flow, $\mathbf{U}_p(\mathbf{x}, t)$, used to satisfy inflow and outflow boundary conditions. The result is

$$\mathbf{U}(\mathbf{x}, t) = \mathbf{U}_p(\mathbf{x}, t) - \frac{1}{4\pi} \sum_{i=1}^{N} \frac{\mathbf{r}_i \times \mathbf{s}_i}{|\mathbf{r}_i|^3} \Gamma_i \phi(|\mathbf{r}_i|/\sigma) \qquad (1)$$

where $\mathbf{r}_i = \mathbf{x} - \mathbf{x}_i$, $\mathbf{x}_i = (\mathbf{x}_i^1 + \mathbf{x}_i^2)/2$, and $\mathbf{s}_i \equiv \mathbf{x}_i^2 - \mathbf{x}_i^1$ is an axial vector along the ith tube. In keeping with the common practice of desingularizing the Biot–Savart law [37], the smoothing function

$$\phi(|\mathbf{r}_i|/\sigma) = 1 - (1 - \tfrac{3}{2}(|\mathbf{r}_i|/\sigma)^3)e^{-(|\mathbf{r}_i|/\sigma)^3} \qquad (2)$$

with σ as a smoothing parameter, appears in the velocity formula. The effect of ϕ is confined to the region $|\mathbf{r}_i| < 2.34\sigma$ because ϕ is essentially unity beyond this point. In practice, very small values of σ, on the order of 10^{-4}, are used so that the main point of the smoothing is to prevent the occurrence of exceptionally large velocities in the unlikely event that the end points of two tubes are in virtually the same spot. Test calculations were performed in which velocity profiles and statistics were computed for a fixed vortex field and differing σ values to gauge the effect of this parameter. It was found that for $\sigma \leq 2 \times 10^{-3}$ any changes to velocity were less than 0.01%. For σ as high as 0.064, a less than 1% variation in the mean statistics was observed.

Evaluation of the velocity at the locations of all vortex tubes via Eq. (1) is an example of an N-body problem and as such requires considerable care in its solution so that the overall method is rendered practical. In fact, a parallel implementation of the Greengard and Rohklin [30] FMM is used that follows the detailed adaptive algorithm set forth by Strickland and Baty [31]. In this, vortices in neighboring boxes contribute to each others' motion via the exact formulas, whereas vortices in more distant boxes are linked via the multipole approximation. The use of smoothing as in Eq. (2) prevents growing the FMM oct tree to its optimal depth containing approximately 100 vortices per box. To prevent loss of efficiency the local FMM evaluation is carried out in this case via a "middleman" scheme based on 3-D linear interpolation from the exact velocities at the corner nodes of the local boxes (and their refinements, if necessary). Because the velocity variation is smooth, the procedure is very accurate.

The FMM as implemented reduces the nominal $\mathcal{O}(N^2)$ cost of evaluating vortex interactions to a far more efficient $\mathcal{O}(N)$. Timings for the evaluation of the sum in Eq. (1) with 16 and 32 parallel processors on a HP Alphaserver ES45 supercomputer are shown in Fig. 1 where in both cases the scaling is linear with N. As will be discussed next, included in these timings is the evaluation of contributions from four image planes of vortices arrayed to either side of the computed mixing layer. Thus, the time needed in evaluating the velocities at the positions of 7 million vortices, which is on the order of 700 s, actually includes the combined effect of 63 million vortices. The timings in the figure are such that complete
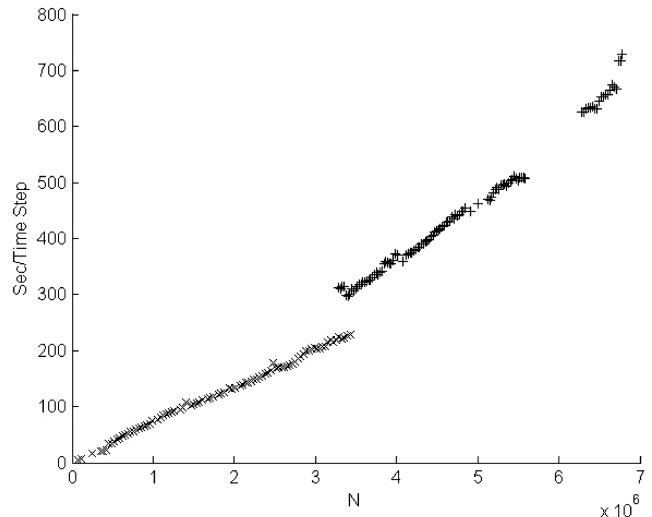

Fig. 1   Cost per time step of velocity evaluation vs number of vortices: +, 16 processors; ×, 32 processors.

simulations of a mixing layer requiring on the order of 1000 iterations can be achieved in a matter of a few days.

III.   Computational Problem

The computational domain used in the simulation of the mixing layer is illustrated in Fig. 2. In this, lengths are scaled by the spanwise period of the flow domain so that the transverse coordinate satisfies $-0.5 \leq z \leq 0.5$. The inlet plane is at $x = 0$, the downstream end is at $x = L$, and y is the vertical coordinate. At the inlet a streamwise velocity profile, $U_{\text{in}}(y)$, is maintained that determines the general scale and dimension of the downstream developing mixing layer. In particular, the momentum thickness [defined in Eq. (7)] at the inlet, θ_0, that is associated with $U_{\text{in}}(y)$ allows the computational domain to be placed into context with the flowfields studied in physical experiments such as that of Bell and Mehta [3] and others where self-similar behavior is seen. By this measure the streamwise extent of the computational domain ranges up to approximately 2000 θ_0, while the spanwise extent is approximately 1000 θ_0, dimensions that are comparable to physical experiments.

Vortex tubes moving beyond L are eliminated as they cross. As indicated above, periodic images of the computational domain to either side are included as part of the velocity field computation. In principle, an infinite number of images should be used, but as this is not practical just a finite number are included. Test computations comparing the flow resulting from 4 vs 32 images to either side show at best a 0.1% effect on the asymptotic streamwise velocity above the mixing layer. It is also the case that the use of four images creates a very slight symmetry about the centerline in the velocity field that all but vanishes with 32 images. Neither of these tendencies affect the quantitative results below, though spanwise flow symmetry will be
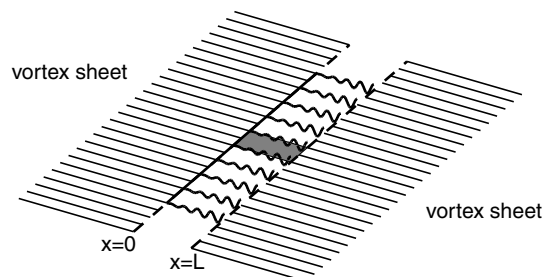

Fig. 2   Schematic of the computed mixing layer. The shaded region, which is of unit width after scaling, is the computational domain. For most computations, four periodic images to each side are used in computing velocities.

seen to have some subtle influences in what occurs in the transition from the laminar inlet field.

Complete specification of the velocity field requires also taking into account the vorticity residing in the regions immediately upstream and downstream of the computational domain. A convenient means of representing such influences is via semi-infinite vortex sheets placed before and after the computational section. The upstream sheet is set to provide a potential flow felt in the computational domain that is consistent with a velocity $U_t = 1$ in the top layer and velocity U_b in the bottom layer. In general it is assumed here that $U_b = 0.6$ matching the experiments of Bell and Mehta [3], though some test calculations have been performed with other values. The vortex sheet placed downstream of the mixing layer (i.e., beyond $x = L$) recovers the influence of vorticity that has exited the computational domain. Although this is a somewhat gross way of taking into account the truncation of the mixing layer, the method adopted here, or some other equivalent technique, is a necessary part of vortex method computations depending on use of the Biot–Savart law.

The imposition of a vortex sheet as a simplified model of the downstream vorticity is felt in several ways, none of which turns out to be of great consequence for the computations. Most obviously, the abrupt change in the vorticity distribution at the downstream end alters the statistics of the turbulent field in a zone abutting $x = L$. In fact, computations show that such effects are not extensive. To give a concrete example, with $L = 2$, the effect of the boundary can be seen in some statistics no further upstream than $x = 1.6$. For the dimensionless units of this study, it will be seen that there still remains a sizable self-similar turbulent flow region that for all intents and purposes is unaffected by the downstream modeling.

Naturally occurring mixing layers have a tendency to displace toward the slower moving fluid, so that placement of the downstream sheet at $y = 0$ is not fully consistent with the position of the downstream extension of the mixing layer that it is designed to replace. For computations in which the downstream sheet is placed at $y = 0$ it was found that, just before $x = L$, the mixing layer has a tendency to turn back up toward $y = 0$. Though the statistical consequences of this are barely noticeable, in the interest of consistency the downstream vortex sheet was displaced a small distance below $y = 0$ so as to more closely align with the missing downstream vortex layers. Preliminary calculations suggested that a small offset of the sheet to $y = -\varepsilon$, where $\varepsilon = 0.01$ is required, and this value was then used in all computations including those discussed here.

With the downstream velocity shift included, the total potential velocity field $\mathbf{U}_p(\mathbf{x}) = (U_p(\mathbf{x}), V_p(\mathbf{x}))$ originating from the upstream and downstream vortex sheets is given by

$$U_p = 0.5(U_t + U_b) + 0.5(U_t - U_b)([\text{sgn}(y)/2 - \arctan(x/y)/\pi]$$

$$+ [\text{sgn}(y + \varepsilon)/2 - \arctan((L - x)/(y + \varepsilon))/\pi]) \quad (3)$$

$$V_p = \frac{U_t - U_b}{4\pi} \log\left(\frac{x^2 + y^2}{(L - x)^2 + (y + \varepsilon)^2}\right) \quad (4)$$

This velocity distribution is used everywhere except in a thin region $0 \leq x \leq 0.01$ where the inlet velocity field is enforced so as to insure that the singularity in Eq. (4) at $x = 0$, $y = 0$ has no effect on nearby vortices. The smoothness of the velocity field near the inlet was not affected by this alteration.

At the start of the calculation the computational region is covered by vortex filaments filling up several parallel layers at different y locations that align with the incoming vorticity field. The filaments on each layer are subdivided into a fixed number of tubes whose circulations are determined by the position the layer has with respect to the inlet velocity. The number of layers equals the number of y positions where new vortex filaments enter the flow at each time step.

The inlet velocity field is taken to be a continuous function ranging from U_b for all points $y \leq y_b < 0$ to U_t for all points $y \geq y_t > 0$. The region between y_b and y_t is subdivided into K layers according to a monotonically increasing set of points y_i, $i = 1, \ldots, K + 1$, with

$y_1 = y_b$ and $y_{K+1} = y_t$. The incoming tubes are centered at the midpoints $(y_i + y_{i+1})/2$, $i = 1, \ldots, K$ as are the vortex sheets spanning the flow domain at the onset of the computation. The initial vortex sheets are subdivided into M filaments of circulation $L(U_{i+1} - U_i)/M$, where $U_i \equiv U_{\text{in}}(y_i)$, $i = 1, \ldots, K + 1$, $U_1 = U_b$, and $U_{K+1} = U_t$. The circulation of the new filament entering the flow domain at the ith layer during the time interval dt is $\Gamma_i = (U_{i+1}^2 - U_i^2)dt/2$.

Regardless of the choice of $U_{\text{in}}(y)$ or the locations of the intermediary points, the total amount of circulation entering the computational domain in each time step is fixed for given parameters U_b, U_t, and dt. The number of layers and how the inlet velocity is divided between them determines how the circulation is distributed. If one layer is used, as for example would be the case if the inlet velocity was taken to be a step function, then the circulation of each tube is significantly higher than if multiple layers associated with a smooth velocity distribution are employed. Even with multiple layers, the fineness of the discretization is affected by how the subdivision is made: for example, if both weak and strong vortices are introduced, then resolution will generally be determined by the strong vortices. Selecting values for y_i that render Γ_i approximately constant for all layers offers perhaps the best strategy for maintaining accuracy of the simulation, a conclusion that is supported to some extent by test calculations. The results presented below are obtained from simulations incorporating an equal distribution of circulation between the vortex layers.

The two choices for $U_{\text{in}}(y)$ shown in Fig. 3 were used in calculations. One is an inlet profile

$$U_{\text{in}}(y) = \begin{cases} U_b(-y/l_b)^{1/7}, & -l_b \leq y < 0 \\ U_t(y/l_t)^{1/7}, & l_t \geq y \geq 0 \end{cases} \quad (5)$$

that crudely approximates the velocity associated with boundary layers produced on either side of a splitter plate. The length parameters here are taken to be $l_t = 0.027$, $l_b = 0.031$ that correspond to how thick the boundary layers would be if the Reynolds number (based on streamwise length) on the top of the splitter plate were $R_x = 500,000$ (see Schlichting [38]). Equation (5) is of a similar type as that used by Tenaud et al. [23] and in very crude fashion by Ashurst and Meiburg [27]. Because the vorticity shedding off each surface has opposite signs, filaments of opposite rotation are brought together in this model. The velocity defect at the inlet disappears as the flow develops downstream.

The second profile in Fig. 3, which was used by Rogers and Moser [7], corresponds to a narrow error function profile in which the distance $y_t - y_b = 0.01$ is quite small. This may be taken as a model of the inlet flow at a location in a mixing layer beyond the point where a velocity defect might exist. It is but one of many ways of replacing a
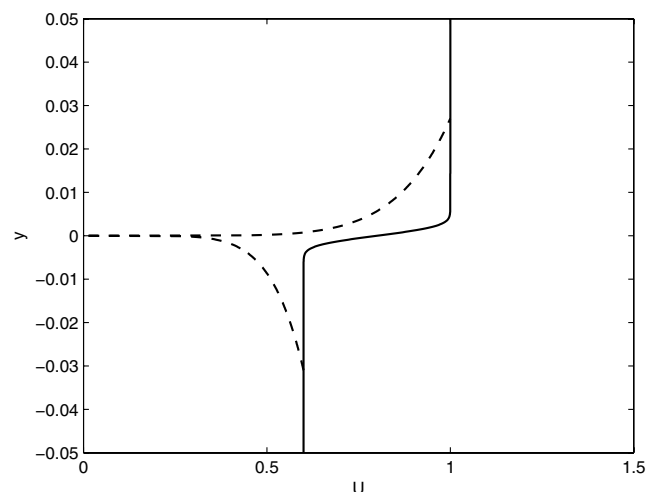

Fig. 3 Inlet velocity fields: solid line, error function; dashed line, boundary layer approximation given by Eq. (5).

step function with a continuous distribution. A number of computations were done using both of the functions displayed in Fig. 3 after which it was observed that there were insufficient differences between the two to warrant separate consideration of both. Consequently, the error function approach is used for the computations described in the present work because it provides superior resolution compared to Eq. (5) for the same number of vorticity layers.

For the calculations in this study the filaments are initially subdivided into either 20 or 25 tubes across the span implying nominal initial tube lengths of 0.05 and 0.04, respectively. The values of h used in computations are generally much smaller than these so that the tubes undergo one or more subdivisions at the very start of the computations until they reach lengths consistent with h. Calculations with as many as 10 layers of filaments have been attempted, with most of the work reported here using eight levels. Some test calculations were performed with just a few layers and relatively large h and these, in keeping with observations of Knio and Ghoniem [29] show a marked decline in the quality of the flow statistics. It appears from the current work that having at least five layers is a minimum requirement for attaining simulations that are not unduly affected by coarse discretization. On the other hand, it is not possible to point to substantial differences in the computations performed using 8 or 10 layers, and so the smaller value is used here in the interest of enhancing computational efficiency.

Many of the following results are taken from two particular simulations: one with $L = 2.0$, $h = 0.025$ and the other with $L = 1.5$, $h = 0.005$. As will become evident, the number of vortex elements in a simulation increases either due to L increasing or h decreasing. The calculations cited below with the smallest values of h generally have $L < 2$ because they are at or near the highest practical resolution for the available computing resources: up to 7 million vortices.

IV. Self-Similarity

Self-similarity in the mixing layer is accompanied by a collapse of the mean velocity profiles at different streamwise locations if plotted in terms of the similarity variable

$$\eta \equiv (y - y_0(x))/l(x) \tag{6}$$

where at each fixed x, $y_0(x)$ is the location where the mean velocity $\bar{U} = (U_t + U_b)/2$ and $l(x)$ is an appropriate length scale that varies in the streamwise direction. In the self-similar region $l(x)$ is expected to be linear and proportional to the momentum thickness [3,39],

$$\theta(x) \equiv \int_{-\infty}^{\infty} (U_t - \bar{U})(\bar{U} - U_b)/(U_t - U_b)^2 \, dy \tag{7}$$

Physical experiments, such as those of Bell and Mehta [3], supported by classical self-similarity arguments assuming the validity of an eddy viscosity model (for an account see [39]) show $\bar{U}$ to be well described by the error function

$$\bar{U} = (U_t + U_b)/2 + erf(\eta)(U_t - U_b)/2 \tag{8}$$

Substituting Eq. (8) into (7) yields

$$\frac{\theta}{l} = \frac{1}{4} \int_{-\infty}^{\infty} (1 - erf(\eta)^2) \, d\eta \tag{9}$$

and after numerically evaluating the right-hand side it is found that

$$\frac{\theta}{l} = 0.399 \tag{10}$$

Equation (8) may be used as it was by Bell and Mehta [3] to determine $l(x)$. In the current study, however, θ is first computed directly from its definition Eq. (7) and then Eq. (10) is used to compute l for use in evaluating η. This approach is made feasible by the fact that, as will be seen below, Eq. (8) is satisfied to high accuracy in the numerical simulations.
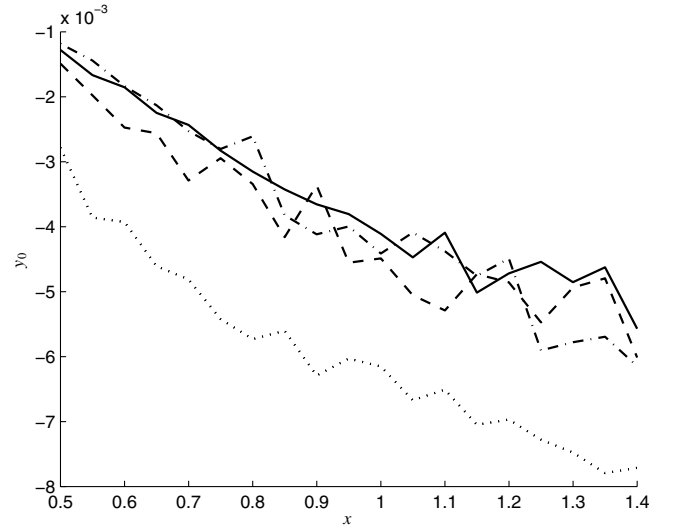

Fig. 4   Streamwise development of y_0. Dotted line, $L = 2$, $h = 0.025$; dashed line, $L = 1.8$, $h = 0.00625$; dash-dotted line, $L = 1.5$, $h = 0.0125$; solid line, $L = 1.5$, $h = 0.005$.

For a given mixing layer simulation $y_0(x)$ may be determined by interpolating between the values of $\bar{U}$ computed on a fine grid. Results from several runs are shown in Fig. 4 where it may be observed that the shift is somewhat sensitive to L at least insofar as where the spatial shift begins to occur. The rate at which the mixing layer moves to the slow side appears to be essentially the same for all cases. It may also be noted that the quantitative shifts in the figure are in alignment with the choice $\varepsilon = 0.01$ used in displacing the downstream vortex sheet as discussed above.

A.   Growth Rate

Figure 5 shows $\theta(x)$ predicted by the current scheme for the calculation with $h = 0.025$ and $L = 2.0$. The growth rate seen here is highly linear and is typical of what is observed in many calculations that were done with differing inlet conditions and parameter values. The slope of $l(x)$ determined from the fitted line depicted in the figure and use of Eq. (10) is 0.0208 which is very much consistent with the range $0.019 \rightarrow 0.023$ observed by Bell and Mehta [3] between tripped and untripped upstream conditions and in other studies such as that of Oster and Wygnanski [40].

A number of calculations were performed with the goal of assessing the dependence of the mixing layer growth rate on numerical parameters. This showed that the only significant effect came from the domain length L, and this dependence vanished once
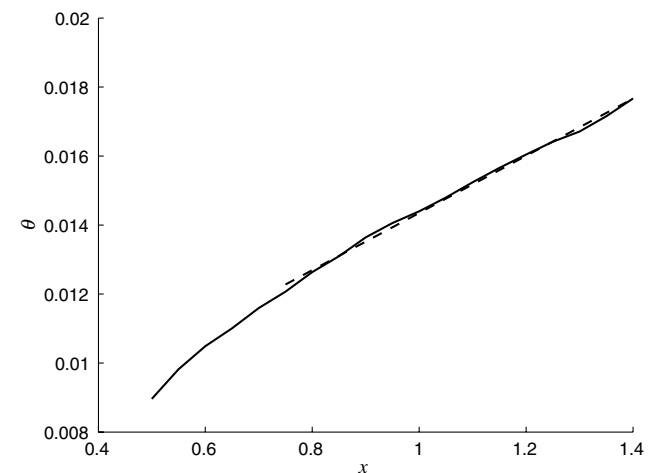

Fig. 5   Momentum thickness, θ. Growth is linear in the self-similar region. The fitted dashed line has a slope of 0.00829 corresponding to $dl/dx = 0.0208$.
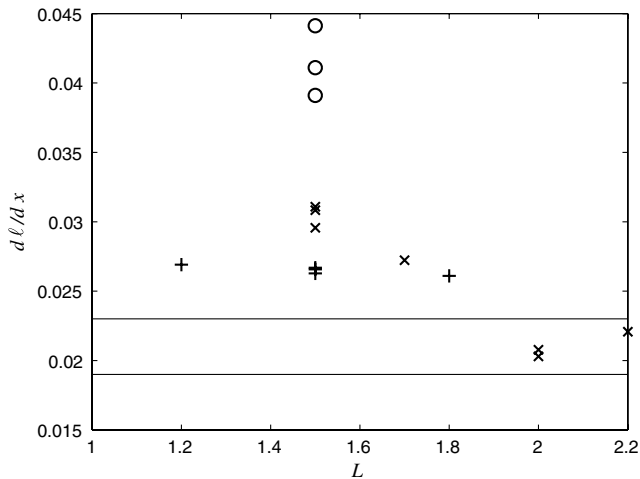
Fig. 6 Dependence of dl/dx on the length of the computational domain. ○, computations with $U_b = 0.5$; ×, computations with $U_b = 0.6$, $h = 0.025$; +, computations with $U_b = 0.6$, $h < 0.025$. Horizontal lines indicate the range seen by Bell and Mehta [3].

Fig. 7 Self-similarity of the mean velocity field. Solid line, $\bar{U}$ at seven locations $0.9 \leq x \leq 1.2$ for a simulation with $L = 1.5$, $h = 0.005$; ○, Eq. (8).

L was large enough. An overview of these results is shown in Fig. 6 where it is seen that the growth rate dl/dx for $L \geq 2$ is within the experimental range as found by Bell and Mehta [3], while for smaller L there appears to be a tendency for overprediction. The trend is particularly evident if just the data with $h = 0.025$ are considered. There is also some indication in the figure that the growth rate decreases with h though this variation is much less than that of L.

Figure 6 also contains some results from calculations with $U_b = 0.5$. These display a substantially higher growth rate than the $U_b = 0.6$ calculation at the same (small) L values. In fact, the trend and quantitative difference between the growth rates at the two U_b values is in accord with the differences measured in physical experiments by Oster and Wygnanski [40].

The general conclusion may be reached that the use of relatively large L is desirable as an antidote to the potentially adverse effects, such as enhanced growth rate, that are attributable to the premature truncation of the downstream turbulent flow domain and its replacement with a simple semi-infinite vortex sheet. On the other hand, as will become clear, the effect of small L appears to be confined to just the growth rate of the mixing layer because neither the appearance of a self-similar region nor its velocity statistics and structural aspects show an obvious influence of this parameter.

As mentioned previously, the value of L does have a strong influence on the number of vortical elements in the computation (and hence its cost) simply because the turbulent flow region is larger and can contain more elements. Depending on the circumstances, this may or may not complicate the opportunity for choosing L large enough to capture the correct growth rate. More on this point will follow once the selection of h is considered, because this parameter also has a strong influence on the number of tubes in a given computation.

B. Velocity Statistics

Mean velocity profiles for the simulation with $L = 1.5$, $h = 0.005$ are shown in Fig. 7 for seven equally spaced locations between $0.9 \leq x \leq 1.2$ in the turbulent self-similar region. The mean of the velocity field is calculated by averaging at intervals of time $\Delta t = 0.1$ from $t = 10.4$ to $t = 18.1$. The profiles are virtually indistinguishable from each other and in very close agreement with the error function in Eq. (8). Predicted mean velocities taken from simulations with other parameter values display similar results.

A representative view of the normal velocity $\bar{V}$ on a vertical cut through the self-similar region is illustrated in Fig. 8. This is qualitatively and quantitatively similar to the results of Druzhinin and Elghobashi [22] and shows the entrainment of fluid from both sides that accompanies the mixing layer growth as well as the downward drift associated with the bending toward the slow speed side. Further insight into the mixing layer growth is provided by
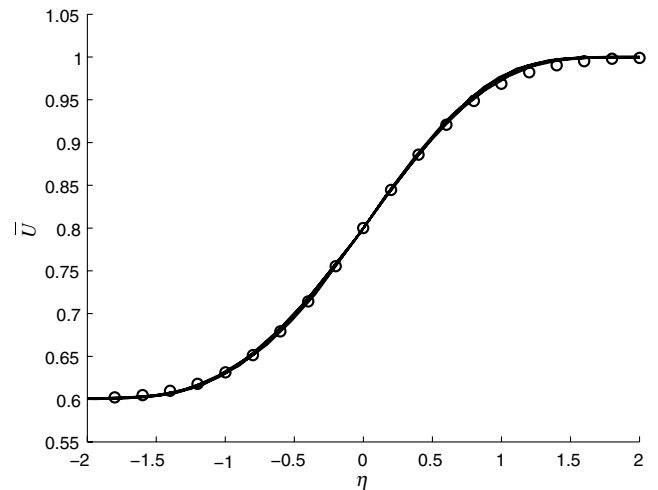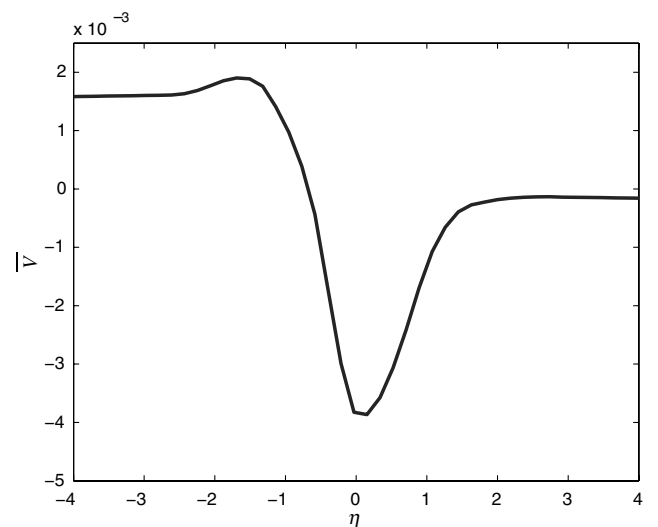

Fig. 8 $\bar{V}$ across the $L = 1.5$, $h = 0.005$ simulation at $x = 0.95$.

Fig. 9 in which the streamlines corresponding to the mean $\bar{U}$, $\bar{V}$ fields are shown. Note that the y coordinate has been greatly expanded in the interest of clarity. The darker line extrapolates to the $x = 0$, $y = 0$ origin of the mixing layer, and thus represents to some approximation the dividing line between flow entering the domain from above and below the splitter plate. Figure 9 makes it clear that straight streamlines accompany the linear growth in thickness. Some idea of how the solution is contaminated near the downstream boundary is revealed in the flattening of the streamlines beyond $x = 1.4$. This supports the previous contention that the simple vortex sheet representation of the missing downstream vorticity has a limited upstream effect on the computed mixing layer.

The self-similarity of the normal and shear Reynolds stresses for the same case as considered in Fig. 7 is shown in Fig. 10. Here, there is also excellent collapse of the statistics albeit with some scatter that likely reflects the need for greater averaging. The accuracy of the predictions is indicated in Fig. 11 where a comparison is made between an appropriate average of the curves in Fig. 10 and the Reynolds stresses measured by Bell and Mehta [3]. The latter are taken from a number of streamwise positions in the self-similar region and show some variation. The present results, though slightly higher than the range seen in the experiments, appear to be good particularly because no attempt was made to duplicate the precise inlet conditions in the experiment.
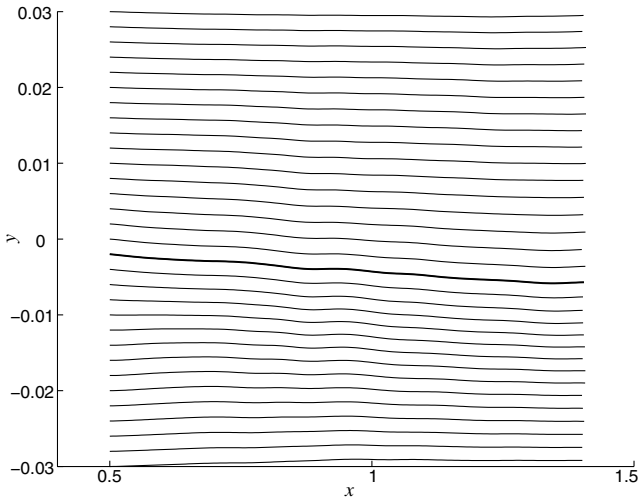
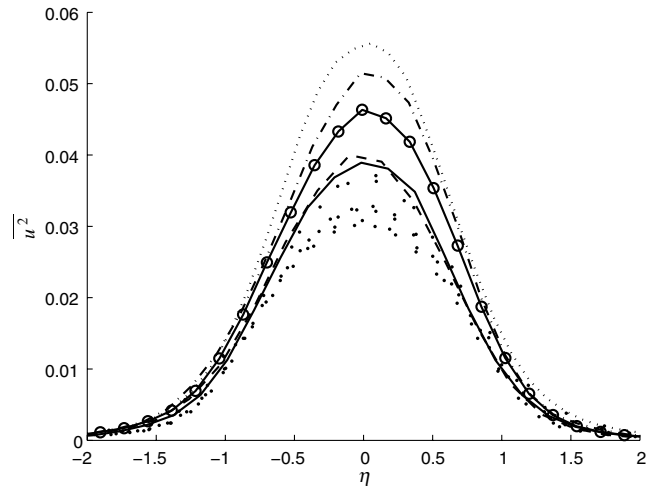**Fig. 9   Streamlines corresponding to $\bar{U}$, $\bar{V}$ for $L = 1.5$, $h = 0.005$ simulation.**

Fig. 12 $\overline{u^2}$ for different h values. Dotted line, $h = 0.025$; dash-dotted line, $h = 0.0125$; $\bigcirc$, $h = 0.00625$; solid line, $h = 0.005$; dashed line, $h = 0.003125$; $\bullet$, data at different streamwise locations from Bell and Mehta [3] experiment.
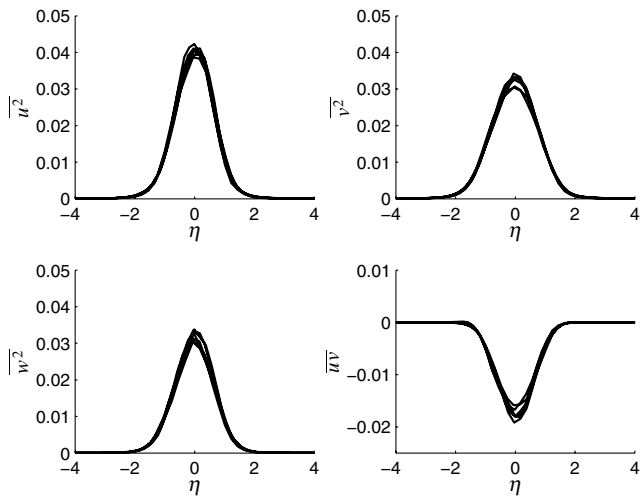

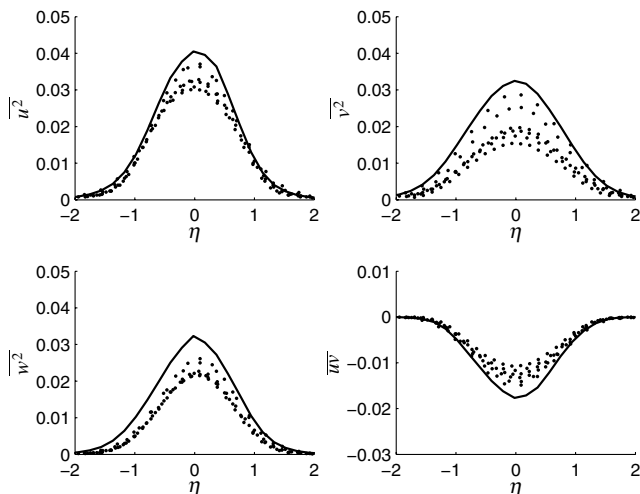**Fig. 10   Reynolds stresses in self-similar region $0.9 \leq x \leq 1.2$.**

Fig. 11   Reynolds stresses compared to data. Symbols are from different streamwise locations in the experiment of Bell and Mehta [3].

a)

b)

Fig. 13   Close-up view of vortex tubes: a), $h = 0.005$; b), $h = 0.025$.

An investigation of how the velocity statistics might depend on the value of h showed the mean velocity to be unaffected while there was a distinct effect on the magnitude of the Reynolds stresses, so long as h was larger than a threshold. This point is illustrated in Fig. 12 where
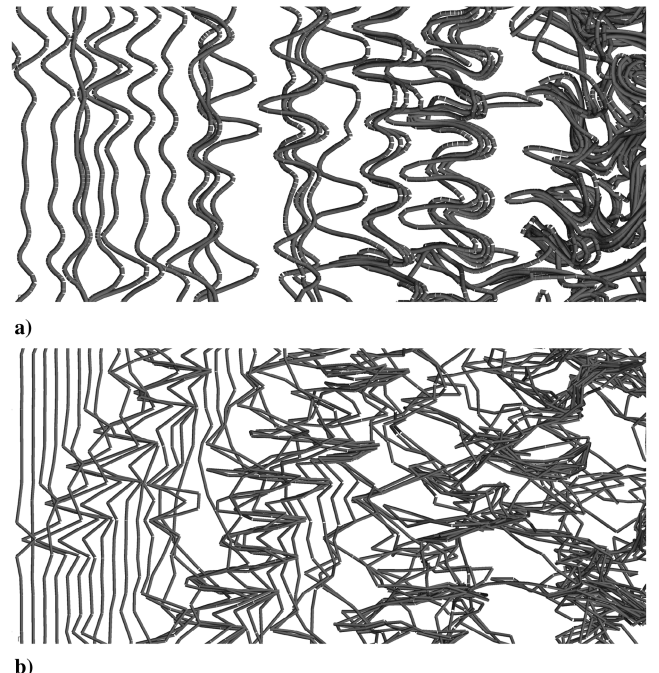
it is seen that the accuracy of the streamwise Reynolds stress significantly improves as h decreases from 0.025 to a value on the order of 0.005. It is also evident that further reduction of h below 0.005 appears to be of little consequence. A likely explanation for this result is contained in Fig. 13 where a comparison is made between the visual appearance of vortex filaments in the simulation with $h = 0.025$ vs the one with $h = 0.005$. The view is from above of small equivalent parts of the mixing layers. In the former case there is an angularity to the filaments that allows the individual straight tubes to be easily discerned, while for the smaller h the angularity is for the most part lost and the filaments appear to be smooth. This result suggests that failure to provide sufficiently fine resolution of the vortex filaments leads to overestimation of the Reynolds stress, at least in the present context of mixing layer flow. Evidently, when h is larger than a threshold the accuracy of the velocity approximation built into Eq. (1) is jeopardized.

The streamwise dependence of the maximum of the normal Reynolds stresses and minimum of the Reynolds shear stress for the

simulation with $L = 1.5$, $h = 0.005$ are shown in Fig. 14. The self-similar region in this case consists, at a minimum, of the domain $0.9 \leq x \leq 1.2$ that was considered previously in Figs. 7 and 10. The growth rate is linear throughout this region and, consistent with expectations of self-similarity, it is evident that the extrema are essentially constant here as well. Beyond $x = 1.2$ the influence of the downstream boundary begins to be felt and may explain the rise in the streamwise Reynolds stress maximum, though evidently, the other three components are not affected in this way. The results in this figure are typical of what occurs in the other simulations.

Another indication of the accuracy of the vortex scheme is provided by the comparisons of the correlation $-\overline{uv}/\sqrt{\overline{u^2}}\sqrt{\overline{v^2}}$ between experiment and computation shown in Fig. 15. The terms in the computed correlations represent averages over the appropriate self-similar regions. Results for three values of h are given where it is seen that all display excellent quantitative agreement with the data including those curves obtained with the larger h. Evidently, the amplitudes of the individual Reynolds stresses are not an issue in this correlation because their influence factors out between the numerator and denominator.
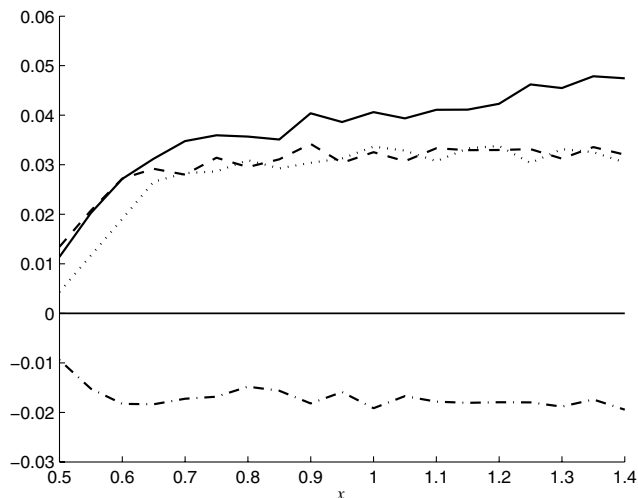

Fig. 14   Streamwise variation of Reynolds stress extrema. Solid line, $\overline{u^2}$; dashed line, $\overline{v^2}$; dotted line, $\overline{w^2}$; dash-dotted line, $\overline{uv}$.
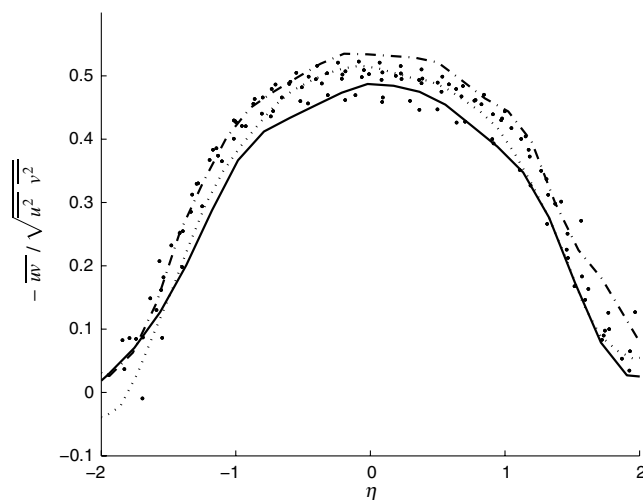

Fig. 15 $-\overline{uv}/\sqrt{\overline{u^2}}\sqrt{\overline{v^2}}$. Dotted line, $L = 2$, $h = 0.025$; dash-dotted line, $L = 1.5$, $h = 0.0125$; solid line, $L = 1.5$, $h = 0.005$; ●, data of Bell and Mehta [3] at different streamwise locations.

V.   Visualizations

The favorable predictions of the previous section suggest that the present high resolution grid-free representation of turbulent flow in terms of vortex filaments is likely to provide a realistic description of the vortical structures at work in the unforced mixing layer. This then provides an opportunity to examine the complete physics of the developing mixing layer from inlet to the self-similar regime, including the late transition into turbulent flow.

A.   General Observations

The vortex filaments that are present in the computational domain at the inception of the mixing layer calculations evolve in the manner of a transient mixing layer while simultaneously convecting gradually beyond the downstream boundary at $x = L$ and hence out of the numerical solution field. In their wake, vortex filaments enter at the inlet boundary and develop over time into a complete spatially growing mixing layer. Figure 16 is a typical view from above of the mixing layer during the startup phase at $t = 1.2$ of a calculation with $L = 2$, $h = 0.025$. Approximately half of the original vortex field is still present in the form of a transient mixing layer in the right half of the image. To the left of this the spatial mixing layer is filling in behind it. The transient layer contains well-defined spanwise roller vortices with associated streamwise rib vortices that may be distinguished from the more heterogeneous vortex pattern on the left-hand side. Between the spatial and transient layers is a large turbulent vortical region whose eventual passage beyond $x = L$ signals the end of the startup phase of the calculation. It may be remarked at this point that this and subsequent figures suggest that the width of the computational domain is more than adequate to not be a factor in shaping the dynamics of the vortical field. Indeed, there are numerous streamwise rib vortices across the span, with many of these appearing to develop independent of each other.

It may be noticed in Fig. 16 that a number of the roller vortices in the transient layer are in the act of merging. The rib vortices show signs of being wrapped around the rollers where they intersect. Moreover, the roller vortices have a tendency to be kinked where they encounter ribs and this aspect continues unabated in the presence of vortex merger. Many of the vortical structures in Fig. 16 are transitioning into turbulence, and as they grow and interact with neighboring vortices turbulence fills the flow domain. The further breakdown into a fully turbulent field is rapid and occurs before the transient mixing layer has fully exited from the computational domain. In many of its observed properties, the dynamics of the transient layer closely follows the observations of prior direct numerical simulations of the transient mixing layer such as that of Rogers and Moser [7].

The vortical structure in the spatial field in Fig. 16 is noticeably different in composition than the transient field it replaces. Later in time, after the transient phase has passed, the vortical pattern visible in the transition region persists in the same general form. In this, strictly spanwise roller vortices are absent in favor of a pattern of oblique roller-type vortices intersecting with riblike vortices. To
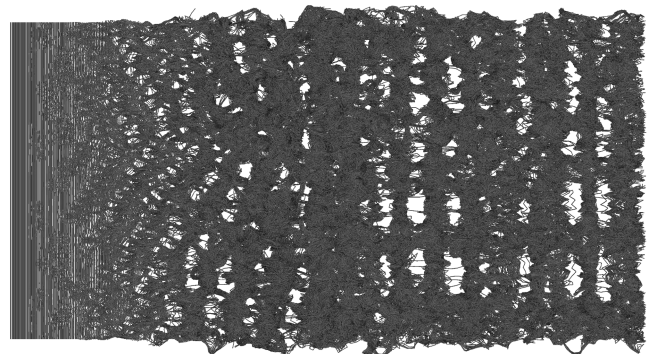

Fig. 16   Top view of mixing layer with $L = 2$, $h = 0.025$ at $t = 1.2$. The flowfield is evenly divided at this time between a transient mixing layer on the right and a developing spatial layer on the left.

some extent this structure contains evidence of partial pairing and branching of vortices reminiscent of the observations of Chandrsuda et al. [13] and Comte et al. [8,9]. It may be also noticed in Fig. 16, and more pronounced in figures to follow, that the mixing layer tends to spread laterally as a natural consequence of turbulent diffusion. This effect is only made visible in the figures because the vortices in neighboring periodic images of the flow domain are not included in the visualizations.

Lest it be thought that the structure in Fig. 16 is in some sense favored in the vortex method, Figs. 17 and 18 corresponding to simulations with $L = 1.5$, $h = 0.005$ and $L = 1.8$, $h = 0.0125$, respectively, show that quite different transitional structures can and do occur. Figure 17 also includes a corresponding side view of the mixing layer so as to give some sense of the growth and proportions that are involved in these computations. In both of the latter figures and most extensively in Fig. 17, the central region of the flow is dominated by the presence of merging spanwise roller vortices interacting with streamwise rib vortices. To either side, and this is most clearly established in Fig. 18, there appears the chain-link fence type of vortex transition that has been seen in the experiments of Nygaard and Glezer [12] and analyzed by Collis et al. [10]. It is interesting to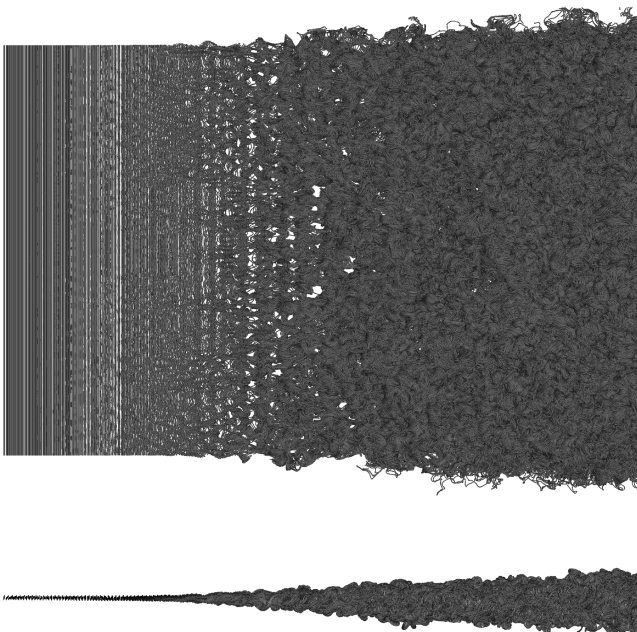 note that the roller/rib and chain-link regimes coexist side by side in the same transitioning flow, albeit the lattice structure begins further upstream than the roller vortex structure and transitions into turbulence earlier. A closer look at the transitional vortex systems in these figures will be given later. Here it suffices to note that what appears to be three different modes of transitional vortices are present in the simulations.

The transitional flows observed in these figures originate from what is ostensibly the identical laminar inlet field. Evidently, the vortex representation is subject to a number of influences that provoke instabilities leading to different vortex arrangements in transition. In view of the quasi symmetry about the central axes that is quite visible in Figs. 17 and 18, it is likely that the symmetric velocity bias created by the use of a relatively small number of periodic extensions has a role to play in what sort of transition structure is present. In particular, roller vortices are found along the central axis of the mixing layer where the velocity is affected equally from the spanwise images while the lattice structure develops near the sides where there is an asymmetric contribution to velocity from the image vortices. In fact, this explanation for the appearance of the lattice structure coincides with the asymmetrical forcing used in obtaining the lattice field in previous experiments [12] and computations [10]. In the present context it is interesting that the velocity asymmetry leading to the chain-link structure is quite small, but evidently not small enough to be overlooked as a perturbation to the vortex field.

One reason why the vortex method might be especially sensitive to small disturbances that promote one or other of the transitional modes is the absence of an explicit model for viscous diffusion. In this case the implied Reynolds number of the simulation is high thus aiding instability. The vortex filament representation also has the property that the effects of small perturbations are initially channeled to the junctures between straight vortex tubes. Small local variations in the computed velocities at these locations begin the instability and the process is self-sustaining. A further complication is the role of upstream feedback in initiating instabilities in ever changing patterns, particularly in the absence of purposeful forcing.

It may be expected that h has some role to play in promoting one form of transition over another. For example, the transitional structures appearing to the left side of Fig. 16 in the spatially developing mixing layer, if equivalent to that observed by Chandrsuda et al. [13], would be associated with turbulent initial conditions. Previously it was seen that turbulence levels are higher for larger h in this simulation so that the flow perhaps reacts more nearly in this case as if the inlet flow were turbulent.

One way that h can affect transition is by influencing where it initiates. To see this, note that h exerts control over the vortex division process in the sense that those vortices whose lengths are close to h are more likely to subdivide in the near future than those that are much smaller than h. Subdivision is important because it provides the filaments with the capability of responding to perturbations along their lengths. Within the fully turbulent field where vortices of many different lengths are present, it is probably not of great consequence that some tubes are closer to subdivision than others, but in the inlet region the opposite is true. In fact, here the tubes share a common length in comparison to h because new filaments entering the domain are divided into tubes of equal length. Thus the behavior of the entire local field of tubes is affected by how close the vortex lengths are to subdivision. If h is incommensurate with the width of the mixing layer, then the newly created tubes are farther from subdivision than if their lengths were commensurate. In the former case computations have a small but noticeable delay in the start of the transition process compared to the latter case. Evidently, tubes that are close to h at the beginning experience their first subdivision more quickly than those that are not and the observed location of transition is affected. By choosing h smaller, any potential delay in the start of the transition process is reduced. For very small h the effect should not be noticeable.

It may be concluded from this discussion that apart from the appearance of the vortex lattice due to spanwise asymmetry in the velocity field, identification of the exact perturbations that promote the vortex scheme to develop into one mode of transition or another is fraught with difficulty: the complexity of the nonlinear system is a

Fig. 17 Top (top) and side (bottom) view of fully developed mixing layer with $L = 1.5$, $h = 0.005$ at $t = 18$.

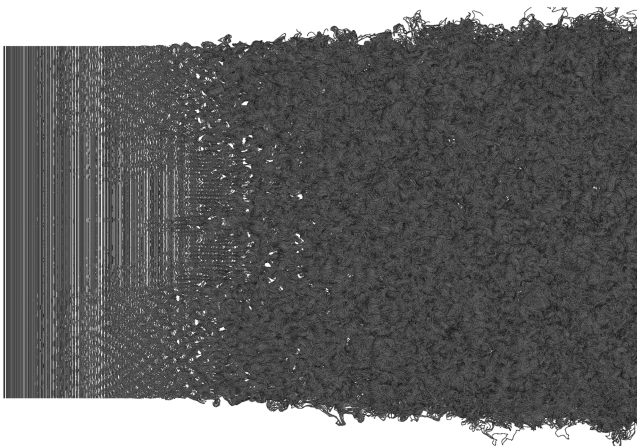**Fig. 18 Top view of mixing layer with $L = 1.8$, $h = 0.0125$ at $t = 5.8$.**

hindrance to such analysis. The fact that the computed solutions do fall into the modes observed in experiments and other computations is an encouraging sign of the physicality of the simulations. It is particularly interesting that the appearance of the various transition modes does not depend on proactively forcing the mixing layer in one substantial way or another: for example, by seeding the flow with upstream turbulence or streamwise vortices. The results suggest that, at least for the high Reynolds number implied in this work, the triggers for the instabilities that grow into one response mode or the other do not have to be large, and aspects of all the transition modes might be present in unforced flows occurring in nature.

B. Vortex Structure

The graphical display of the field of computational elements in a vortex method affords a view of vortical flow features that is free of some of the ambiguities present in the interpretation of photographic images from physical experiments or the plotting of 3-D isosurfaces in grid-based simulation methods. This quality enabled the analysis of the preceding section and now it is used to take a closer look at some of the important dynamical aspects of the transition and turbulent flow regions. A particularly clear view of the dichotomy between the roller/rib vs lattice mode of transition is given in Fig. 19 that is a magnified view of the image in Fig. 18 wherein only the vortices that entered the flow at one of the eight layers are shown. The lattice structure is plainly revealed and seen to match the images reported by Comte et al. [8,9] and Collis et al. [10]. Seemingly unaffected by the vortex lattice is the adjacent roller and rib vortex pattern. The contrast between the ways in which neighboring vortex filaments interact in each of the two modes of transition is striking.

The view of the roller and rib vortices in Fig. 19 makes especially clear the vortex merging and secondary instabilities leading to the twisting vortex filaments. The three dimensionality of the vortex
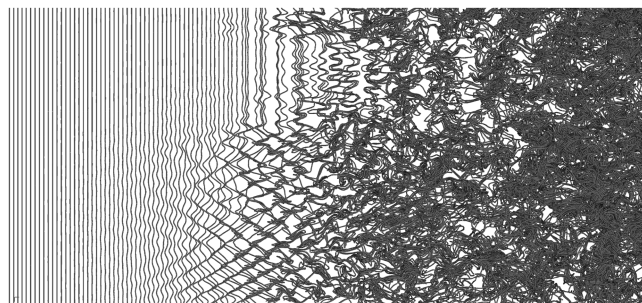
dynamics in the transition is emphasized in Fig. 20 which is a closeup from above and the side of the vortices in one layer taken from Fig. 17. As observed by Bell and Mehta [3] the tendency to the formation of streamwise vortices precedes the appearance of the first roller. The side view of the vortices shows that even the earliest perturbations are three dimensional wherein the filament is accelerated where it bends up and decelerated where it bends down. In many instances neighboring filaments distort in phase with each other. Where they do not, filaments may overtake downstream filaments and be overtaken by upstream filaments.

An interesting aspect of the visualization is to see what might be learned about the late transition and how this might vary between the several modes. Figures 21 and 22 are close-up views of the vortical field in Figs. 17 and 18, respectively, while Fig. 23 contains side view plots of vortex tubes taken from narrow slices through the mixing layers. To the left side in Fig. 21 are the roller vortices developing through a merger interlaced with growing rib vortices. Vortex mergers are clearly visible in Fig. 23a in the vicinity of $x = 0.47$, 0.55, 0.58, 0.64, and 0.70 with obvious braid regions at $x = 0.49$, 0.53, and 0.61. The downstream end of Fig. 21 is at approximately $x = 0.8$ and the braid region at $x = 0.61$ is clearly visible at the center of the figure where large streamwise vortices connect an upstream roller with merging downstream rollers. The comparable view in Fig. 22 shows a precise diamond-shaped pattern of interlocking vortices in the form of a chain-link fence. Not surprisingly, the corresponding image in Fig. 23b gives a very different vortex profile than is associated with the roller/ribs.

The view toward the right side in Figs. 21 and 22 as well as in Fig. 23 shows the downstream evolution of the organized transitional structures in the rib/roller and lattice modes. In Fig. 21 the roller vortices continue to merge and grow in size as they interact with increasingly large rib vortices. Some degree of spanwise organization to the flow persists as the vortices acquire the more and more chaotic appearance of a complex turbulent field of interacting vortical structures. This scenario is reflected in the changes in Fig. 23a between $x = 0.6$, where clearly defined roller/braids are present, to $x = 0.75$ where there are still objects that have the appearance of rollers albeit distorted, to points downstream of $x = 0.85$ where roller vortices are no longer evident. In effect, the rollers exert some influence as coherent structures inside the

Fig. 19 Close-up of one layer of vortices in the mixing layer with $L = 1.8$, $h = 0.0125$ at $t = 5.8$.

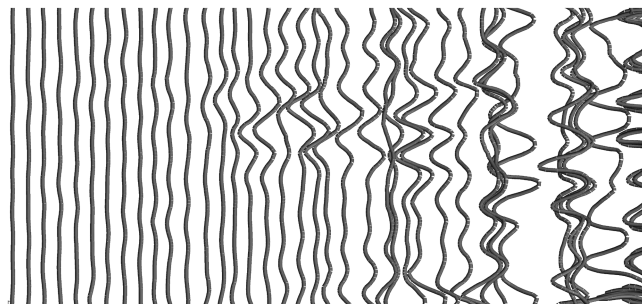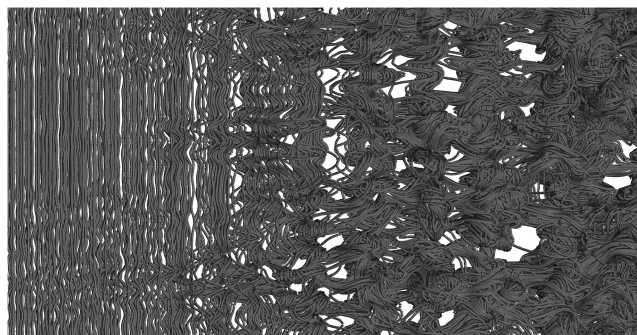**Fig. 20 Close-up from top (top) and side (bottom) of one layer of vortices from the mixing layer in Fig. 17.**

Fig. 21 Enlarged view of the vortex structure in Fig. 17.
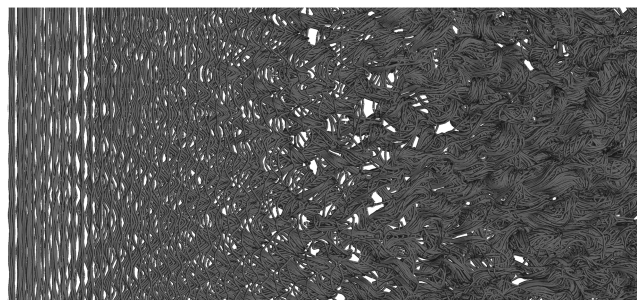

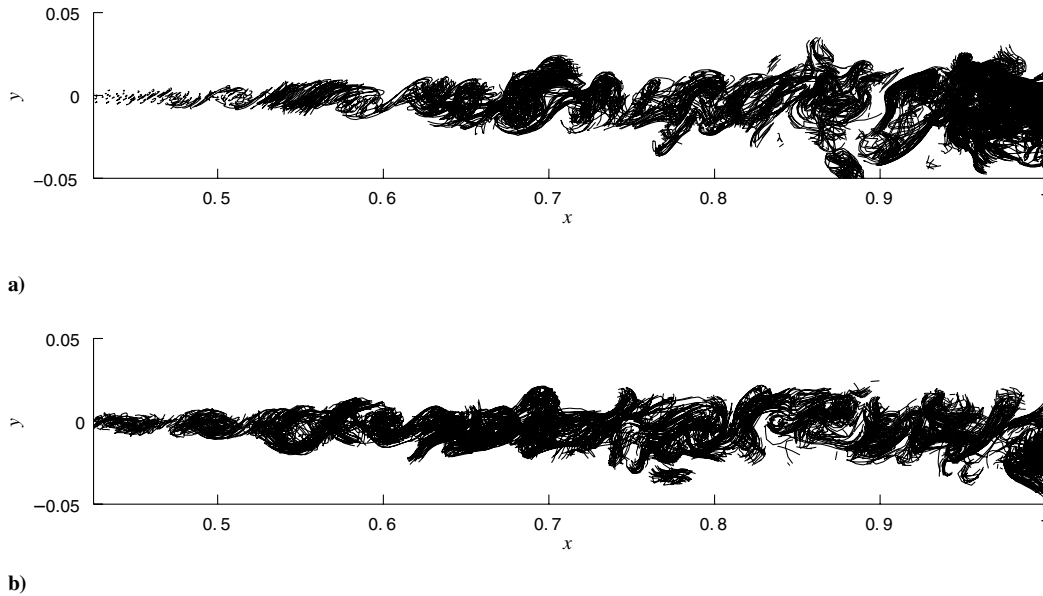**Fig. 22 Enlarged view of the vortex structure in Fig. 18.**

a)

b)

Fig. 23   Side view of vortices. a) Tubes for which $-0.01 \leq z \leq 0.01$ corresponding to Fig. 21; b) tubes for which $-0.31 \leq z \leq -0.29$ corresponding to Fig. 22.

turbulent field, approximately the extent of two rollers, before they are subsumed by the turbulent motion. Under different inlet conditions, however, it is not difficult to imagine that stronger roller vortices would persist further into the turbulent field, such as is the case in the experiments of Brown and Roshko [41] or the forced simulations of Rogers and Moser [7].

The late stage of the vortex lattice transition in Fig. 22 appears as a natural extension of the preceding structure. In this, the individual vortices have a tendency to grow larger and interact with neighboring vortices until the chain-link pattern is indistinct and the entire field is filled with vortices. Viewed from the side in Fig. 23b the growth in the lattice structure is visible upstream of $x = 0.6$ followed by a rapid dissolution into turbulence beyond this point. Consistent with Figs. 18 and 19 the onset of turbulence in Fig. 23b is farther upstream than in Fig. 23a. In both transition modes, the growing size and complexity of the structures appears to be associated in part with vortex filaments winding around the transitional vortices. Although the final turbulent fields are replete with randomly interacting structures, in the form of agglomerations of parallel filaments, these are of a scale no larger than is achieved at the end of transition.

Some idea of the behavior of individual vortex filaments within the mixing layer simulations is provided by Fig. 24 showing vortices at different streamwise locations for the flow with $L = 1.5$, $h = 0.005$. The filaments toward the downstream end of the image have undoubtedly been simplified via the removal of vortex loops. Where transition begins the instability of the vortical field is visible in the
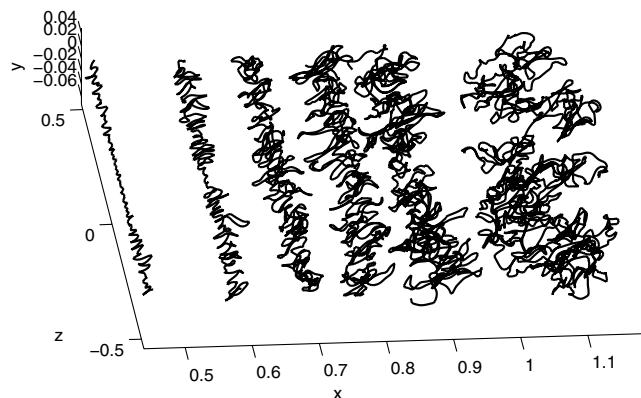

Fig. 24   Representative vortex filaments at different streamwise positions in the mixing layer with $L = 1.5$, $h = 0.005$ at $t = 18$.

wiggling of the vortex filaments and their elongation consistent with Fig. 20. The final transition to turbulence is reflected in the loss of spanwise coherence to the filaments and their very rapid spread to encompass a large region of the flow. The last filament in the figure is fully within the self-similar turbulent zone, and its complexity mirrors that of the overall turbulent field.

VI.   Conclusions

A grid-free vortex filament method has been applied to the simulation of the spatially developing, unforced, shear layer over a domain sufficient to include a substantial self-similar region. Key requirements for enabling these high resolution computations filled with many millions of elements was an efficient implementation of the FMM and the incorporation of loop removal to control growth in the number of vortex elements produced by stretching. The growth rate of the mixing layer showed some sensitivity to the length of the computational domain, but once a threshold was passed, the scheme reproduced experimental values. Similarly, the accuracy of Reynolds stress predictions was enhanced by imposing a sufficiently small upper bound to the length of the vortex tube elements: one that provided for the smoothness of the vortex filaments. In all cases, the mean velocity field in the self-similar flow regime was very well predicted to be an error function.

Accompanying the favorable flow statistics was an underlying transitional vortical structure that is largely familiar from previous experimental and numerical studies. An interesting result, that may be associated with the tacit high Reynolds number of the simulations, was the subtlety with which small perturbations in the implementation of the numerical scheme led to the appearance of one or another of the vortical transition modes. Such behavior may be regarded as consistent with the well-known sensitivity of mixing layers to a wide range of stimuli. In the present case, a slight spanwise bias to the velocity field appeared to be a definite factor in influencing the transition to take on the chain-link fence configuration, though determining the complete cause and effect in this and the other cases is a formidable undertaking.

The simulations have given a detailed view of the behavior of the vorticity field from the inlet to the turbulent self-similar region. The onset of turbulence after the roller/rib vortex transition differed somewhat from that following the lattice structure. The formation of roller vortices was noted to occur a small distance downstream of the position where the lattice transition initiates and the coherence associated with large roller vortices at the end of transition persisted a short way into the fully turbulent flow. For both transition regimes

the breakdown of structures into turbulence follows their growth aided by the winding of vortex filaments and an escalation of their interactions with neighboring structures.

The present scheme may serve as a basis for studying many additional aspects of the mixing layer such as predicting the behavior of dispersed particles. Indeed, the special capability of the method in representing vortical structure at a range of scales that underlies turbulent mixing should be of considerable benefit in accurately modeling particle laden flows.

Acknowledgments

References

[1] Lasheras, J. C., Cho, J. S., and Maxworthy, T., "On the Origin and Evolution of Streamwise Vortical Structures in a Plane, Free Shear Layer," *Journal of Fluid Mechanics*, Vol. 172, 1986, pp. 231–258.
doi:10.1017/S0022112086001726

[2] Lasheras, J. C., and Choi, H., "Three-Dimensional Instability of a Plane Free Shear Layer: An Experimental Study of the Formation and Evolution of Streamwise Vortices," *Journal of Fluid Mechanics*, Vol. 189, 1988, pp. 53–86.
doi:10.1017/S0022112088000916

[3] Bell, J., and Mehta, R., "Development of a Two-Stream Mixing Layer from Tripped and Untripped Boundary Layers," *AIAA Journal*, Vol. 28, No. 12, 1990, pp. 2034–2042.

[4] Leboeuf, R. L., and Mehta, R. D., "Vortical Structure Morphology in the Initial Region of a Forced Mixing Layer: Roll-Up and Pairing," *Journal of Fluid Mechanics*, Vol. 315, 1996, pp. 175–221.
doi:10.1017/S002211209600239X

[5] Slessor, M. D., Bond, C. L., and Dimotakis, P. E., "Turbulent Shear-Layer Mixing at High Reynolds Numbers: Effects of Inflow Conditions," *Journal of Fluid Mechanics*, Vol. 376, 1998, pp. 115–138.
doi:10.1017/S0022112098002857

[6] Rogers, M. M., and Moser, R. D., "The Three-Dimensional Evolution of a Plane Mixing Layer: The Kelvin-Helmholtz Rollup," *Journal of Fluid Mechanics*, Vol. 243, 1992, pp. 183–226.
doi:10.1017/S0022112092002696

[7] Rogers, M. M., and Moser, R. D., "Direct Simulation of a Self-Similar Turbulent Mixing Layer," *Physics of Fluids*, Vol. 6, No. 2, 1994, pp. 903–923.
doi:10.1063/1.868325

[8] Comte, P., Lesieur, M., and Lamballais, E., "Small-Scale Stirring of Vorticity and a Passive Scalar in a 3D Temporal Mixing Layer," *Physics of Fluids A*, Vol. 4, No. 12, 1992, pp. 2761–2778.
doi:10.1063/1.858334

[9] Comte, P., Silvestrini, J. H., and Begou, P., "Streamwise Vortices in Large-Eddy Simulations of Mixing Layers," *European Journal of Mechanics. B, Fluids*, Vol. 17, No. 4, 1998, pp. 615–637.
doi:10.1016/S0997-7546(98)80016-2

[10] Collis, S. S., Lele, S. K., Moser, R. D., and Rogers., M. M., "The Evolution of a Plane Mixing Layer with Spanwise Nonuniform Forcing," *Physics of Fluids*, Vol. 6, No. 1, 1994, pp. 381–396.
doi:10.1063/1.868035

[11] Ansari, A., "Self-Similarity and Mixing Characteristics of Turbulent Mixing Layers Starting from Laminar Initial Conditions," *Physics of Fluids*, Vol. 9, No. 6, 1997, pp. 1714–1728.
doi:10.1063/1.869288

[12] Nygaard, K., and Glezer, A., "The Effect of Phase Variations and Cross-Shear on Vortical Structures in a Plane Mixing Layer," *Journal of Fluid Mechanics*, Vol. 276, 1994, pp. 21–59.
doi:10.1017/S0022112094002454

[13] Chandrsuda, C., Mehta, R. D., Weir, A. D., and Bradshaw, P., "Effect of Free-Stream Turbulence on Large Structure in Turbulent Mixing Layers," *Journal of Fluid Mechanics*, Vol. 85, No. 4, April 1978, pp. 693–704.
doi:10.1017/S0022112078000877

[14] Dimotakis, P. E., "Turbulent Free Shear Layer Mixing and Combustion," *High Speed Flight Propulsion Systems*, Vol. 137,

[15] Balaras, E., Piomelli, U., and Wallace, J. M., "Self-Similar States in Turbulent Mixing Layers," *Journal of Fluid Mechanics*, Vol. 446, 2001, pp. 1–24.

[16] Bernard, P. S., "Turbulent Flow Properties of Large Scale Vortex Systems," *Proceedings of the National Academy of Sciences of the United States of America*, Vol. 103, No. 27, June 2006, pp. 10174–10179.
doi:10.1073/pnas.0604159103

[17] Dimotakis, P. E., "Two-Dimensional Shear-Layer Entrainment," *AIAA Journal*, Vol. 24, No. 11, 1986, pp. 1791–1796.

[18] Koochesfahani, M. M., and Dimotakis, P. E., "Mixing and Chemical Reactions in a Turbulent Liquid Mixing layer," *Journal of Fluid Mechanics*, Vol. 170, 1986, pp. 83–112.
doi:10.1017/S0022112086000812

[19] Lowery, P. S., and Reynolds, W. C., "Numerical Simulation of a Spatially-Developing, Forced, Plane Mixing Layer," Stanford University, Mechanical Engineering Department, Rept. TF-26, 1986.

[20] Leboeuf, R. L., and Mehta, R. D., "On Using Taylor's Hypothesis for Three-Dimensional Mixing Layers," *Physics of Fluids*, Vol. 7, No. 6, 1995, pp. 1516–1518.
doi:10.1063/1.868539

[21] Delville, J., Ukeiley, L., Cordier, L., Bonnet, J. P., and Glauser, M., "Examination of Large-Scale Structures in a Turbulent Plane Mixing Layer. Part 1. Proper Orthogonal Decomposition," *Journal of Fluid Mechanics*, Vol. 391, 1999, pp. 91–122.
doi:10.1017/S0022112099005200

[22] Druzhinin, O. A., and Elghobashi, S. E., "Direct Numerical Simulation of a Three-Dimensional Spatially Developing Bubble-Laden Mixing Layer with Two-Way Coupling," *Journal of Fluid Mechanics*, Vol. 429, 2001, pp. 23–61.
doi:10.1017/S0022112000002603

[23] Tenaud, C., Pellerin, S., Dulieu, A., and Ta Phuoc, L., "Large Eddy Simulations of a Spatially Developing Incompressible 3D Mixing Layer Using the v-ω Formulation," *Computers and Fluids*, Vol. 34, 2005, pp. 67–96.
doi:10.1016/j.compfluid.2004.03.003

[24] Bernard, P. S., Collins, J. P., and Krispin, J., "Gridfree Simulation of Turbulent Boundary Layers Using Vorcat," AIAA Paper 2003-3424, 2003.

[25] Bernard, P. S., Potts, M. A., and Krispin, J., "Studies of Turbulent Mixing Using the Vorcat Implementation of the 3D Vortex Method," AIAA Paper 2003-3599, 2003.

[26] Bernard, P. S., Collins, J. P., and Potts, M., "Vortex Method Simulation of Ground Vehicle Aerodynamics," *SAE Transactions Journal of Passenger Cars—Mechanical Systems*, 2005, pp. 612–624.

[27] Ashurst, W. T., and Meiburg, E., "Three-Dimensional Shear Layers via Vortex Dynamics," *Journal of Fluid Mechanics*, Vol. 189, 1988, pp. 87–116.
doi:10.1017/S0022112088000928

[28] Inoue, O., "Vortex Simulation of Spatially Growing Three-Dimensional Mixing Layers," *AIAA Journal*, Vol. 27, No. 11, 1989, pp. 1517–1523.

[29] Knio, O. M., and Ghoniem, A. F., "The Three-Dimensional Structure of Periodic Vorticity Layers Under Non-Symmetric Conditions," *Journal of Fluid Mechanics*, Vol. 243, 1992, pp. 353–392.
doi:10.1017/S0022112092002751

[30] Greengard, L., and Rohklin, V., "A Fast Algorithm for Particle Simulations," *Journal of Computational Physics*, Vol. 73, No. 2, 1987, pp. 325–348.
doi:10.1016/0021-9991(87)90140-9

[31] Strickland, J. H., and Baty, R. S., "A Three Dimensional Fast Solver for Arbitrary Vorton Distributions," Sandia National Laboratory, TR SAND93-1641, 1993.

[32] Koumoutsakos, P., and Leonard, A., "High-Resolution Simulations of the Flow Around an Impulsively Started Cylinder Using Vortex Methods," *Journal of Fluid Mechanics*, Vol. 296, 1995, pp. 1–38.
doi:10.1017/S0022112095002059

[33] Ploumhans, P., Winckelmans, G. S., Salmon, J. K., Leonard, A., and Warren, M. S., "Vortex Methods for Direct Numerical Simulation of Three-Dimensional Bluff Body Flows: Application to the Sphere at $Re = 300$, 500, and 1000," *Journal of Computational Physics*, Vol. 178, No. 2, 2002, pp. 427–463.
doi:10.1006/jcph.2002.7035

[34] Cottet, G.-H., Michaux, B., Ossia, S., and VanderLinden, G., "A Comparison of Spectral and Vortex Methods in Three-Dimensional Incompressible Flows," *Journal of Computational Physics*, Vol. 175, No. 2, 2002, pp. 702–712.

doi:10.1006/jcph.2001.6963

[35] Chorin, A. J., "Hairpin Removal in Vortex Interactions 2," *Journal of Computational Physics*, Vol. 107, No. 1, 1993, pp. 1–9.
doi:10.1006/jcph.1993.1120

[36] Chorin, A. J., *Vorticity and Turbulence*, Springer–Verlag, New York, 1994, pp. 152–155.

[37] Puckett, E. G., "Vortex Methods: An Introduction and Survey of Selected Research Topics," *Incompressible Computational Fluid Dynamics: Trends and Advances*, edited by M. D. Gunzburger, and R. A. Nicolaides, Cambridge Univ. Press, Cambridge, England, U.K., 1993, pp. 335–407.

[38] Schlichting, H., *Boundary Layer Theory*, 7th ed., McGraw–Hill, New York, 1979.

[39] Bernard, P. S., and Wallace, J. M., *Turbulent Flow: Analysis, Measurement and Prediction*, Wiley, Hoboken, 2002.

[40] Oster, D., and Wygnanski, I., "The Forced Mixing Layer Between Parallel Streams," *Journal of Fluid Mechanics*, Vol. 123, 1982, pp. 91–130.
doi:10.1017/S0022112082002973

[41] Brown, G. L., and Roshko, A., "On Density Effects and Large Structure in Turbulent Mixing Layers," *Journal of Fluid Mechanics*, Vol. 64, No. 4, July 1974, pp. 775–816.
doi:10.1017/S002211207400190X

X. Zhong
Associate Editor